Characterizing the Composition of Sand and Mud Suspensions in Coastal & Estuarine Environments using Combined Optical and Acoustic Measurements

Stuart G. Pearson[1,2], Romaric Verney[3], Bram C. van Prooijen[1], Duc Tran[3], Erik C.M. Hendricks[1,2], Matthias Jacquet[3], and Zheng Bing Wang[2,1]

[1]Faculty of Civil Engineering and Geosciences, Delft University of Technology, PO Box 5048, 2600GA Delft, the Netherlands

[2]Deltares, P.O. Box 177, 2600MH Delft, the Netherlands

[3]IFREMER, 1625 Route de Sainte-Anne, 29280 PlouzanÃĪ, France

Key Points:

- Suspended sand and mud can be distinguished by their different optical and acoustic backscatter signatures
- We define a sediment composition index (SCI) from relative optical and acoustic backscatter and verify it with lab and field measurements
- SCI can be used to estimate the fraction of suspended sand, adding interpretive value to measurements in mixed sediment environments

Corresponding author: Stuart G. Pearson, `s.g.pearson@tudelft.nl`

Abstract

Quantifying and characterizing suspended sediment is essential to successful monitoring and management of estuaries and coastal environments. To quantify suspended sediment, optical and acoustic backscatter instruments are often used. Optical backscatter systems are more sensitive to fine particles ($< 63\mu m$) and flocs, whereas acoustic backscatter systems are more responsive to larger sand grains ($> 63\mu m$). It is thus challenging to estimate the relative proportion of sand or mud in environments where both types of sediment are present. The suspended sediment concentration measured by these devices depends on the composition of that sediment, so it is also difficult to measure concentration with a single instrument when the composition varies. The objective of this paper is to develop a methodology for characterizing the relative proportions of sand and mud in mixed sediment suspensions by comparing the response of simultaneous optical and acoustic measurements. We derive a sediment composition index (SCI) that can be used to directly predict the relative fraction of sand in suspension. Here we verify the theoretical response of these optical and acoustic instruments in laboratory experiments, and successfully apply this approach to field measurements on the ebb-tidal delta of Ameland Inlet in the Netherlands. Increasing sand content decreases SCI, which was verified in laboratory experiments. A reduction in SCI is seen under more energetic conditions when sand resuspension is expected. Conversely, the SCI increases in calmer conditions when sand settles out, leaving behind finer sediment. This approach provides crucial knowledge of suspended sediment composition in mixed sediment environments.

Plain Language Summary

Sand and mud particles are the building blocks of our coastlines. Counting and describing sand and mud particles floating through the water is essential to managing coasts. We commonly do this with devices that send out a sound (acoustic) or light (optical) signal into the water. The sensors measure the strength of the signal reflecting back off of any sand and mud particles passing by. Optical instruments are better at “seeing” mud than sand, and acoustic instruments are better at “hearing” sand than mud. If both sand and mud are present, a single instrument will not accurately estimate the total amount of sediment because of these different sensitivities. Instead, we can use both types of instrument together and compare what we “see” with what we “hear”. This comparison allows us to estimate whether there are more sand or mud particles floating through the water. The

relationship between "seeing" and "hearing" can be described in a single number, the sediment composition index (SCI). We successfully tested this approach in laboratory experiments and then applied it to a site on the coast of the Netherlands. This approach gives us a new way to understand environments that are both sandy and muddy.

1 Introduction

1.1 Background

Estuaries and coastal seas are characterized by strong morphological and sedimentary gradients, from shallow beaches and intertidal shoals or flats, to deeper foreshore and channel areas or other subtidal features. Furthermore, the sediment composition at a given site may vary widely in both particle size and mineralogy [*Winkelmolen and Veenstra*, 1974; *Flemming and Ziegler*, 1995; *Son et al.*, 2011]. The size and material properties of fine sediment (a.k.a. "fines" or "mud") and sand are different: sand particles are individual quasi-spherical grains (with typical density $\rho_s = 2,650 kg/m^3$ for quartz particles), between 63 and $2,000 \mu m$ in diameter, d. Fine sediments, especially clay particles ($d < 2 \mu m$), have the ability to flocculate and often bond with organic matter. The resulting flocs vary widely in diameter (from 10 to $1,000 \mu m$) and have relatively low densities ($\rho_{floc} = O(1,100 - 2,000 kg/m^3)$) with irregular shapes and lower settling velocities than sand [*Chapalain et al.*, 2019; *Many et al.*, 2019]. The spatial distribution of these different types of sediment is a function of morphology, supply, and hydrodynamic conditions.

Due to episodic (storms and floods) and persistent (tides) hydro-meteorological forcing and human influences, estuarine and coastal sediment are highly dynamic. Bed sediments are mobilized and transported, through bed load (rolling, sliding, and saltating near the surface of the seabed) or suspended load (held aloft in the water column by turbulence). In this paper we focus on transport in suspension, dealing with fine sediments or mud ($d < 63 \mu m$) and very fine to medium sand $d = 63 - 500 \mu m$, the latter being found in suspension (relatively close to the bed) during energetic conditions. Depending on local and remote bed composition and hydrodynamic forcing, the concentration and nature of suspended particulate matter (SPM) will drastically change.

The main challenge faced in understanding coastal sediment dynamics and quantifying associated fluxes is thus to make continuous observations of total (sand and mud) suspended sediment and their related mass concentration (SSC). Continuous *in situ* measurements are possible with acoustic or optical instruments [*Fettweis et al.*, 2019], but their measurement capabilities are inextricably tied to the material properties of the sediment they observe. Each type of instrument responds with different sensitivity to fine or sandy sediment because of a dependence on particle size and density. Hence, in practice, calibration models for optical or acoustic sensors are built against *in situ* samples, the latter providing reference gravimetric concentration. However, these models are representative of a given condition (e.g., calm, moderate tidal flows with SPM dominated by fine sediments), and are not well-adapted for observing a succession of low- and high-energy conditions when the SPM sand and mud content (f_{sand} and f_{mud}) can vary strongly in time. The most appropriate methodology would require sampling and re-calibrating sensors as fast as SPM composition changes, but this is neither easily predictable nor realistic. A library of population-adapted calibration models could be built following *Green and Boon* [1993], but knowledge about SPM composition dynamics is a prerequisite for their application.

In this context, we propose an original sediment composition index (SCI) derived from optical and acoustic measurements to quantitatively and dynamically evaluate the relative fraction of sand or fine sediments in suspension. The concept is first validated using laboratory measurements, and then applied to field measurements.

1.2 Optical Backscatter Measurements

Optical Backscatter (OBS) sensors are widely used to indirectly measure suspended sediment concentration. Near-infrared light (typical wavelength $\lambda = 0.780 - 0.865\mu m$) is emitted from the instrument, backscattered by suspended particles, and then recorded by photoreceptors. In a Mie scattering regime, backscatter is strongest when the light wavelength and particle size are similar, so OBS are more sensitive to fine sediment particles $O(1\mu m)$ than sand particles $O(100\mu m)$ [*Green and Boon*, 1993; *Conner and De Visser*, 1992; *Voulgaris and Meyers*, 2004]. According to *Sutherland et al.* [2000], the photon flux received by the sensor is given as:

$$F = VNE\frac{\pi d^2}{4}Q_s \tag{1}$$

Where F is photon flux $[W]$, V is scattering volume $[cm^3]$, N is the number concentration of scatters $[cm^{-3}]$, E emitted irradiance $[W/cm^2]$, d is the particle diameter $[\mu m]$, Q_s the (back)scattering efficiency of the particles $[-]$. Relating the number concentration to the mass concentration SSC $[mg/L]$, this relationship can be modified as follows [*Sutherland et al.*, 2000]:

$$F = \frac{3}{2}\frac{V(SSC)E}{\rho_s d}Q_s \tag{2}$$

Where ρ_s is the particle (dry) density $[kg/m^3]$. This flux is then translated to a voltage output by the sensor.

Equation 2 can then be reworked as:

$$OBS = \alpha_{OBS}\frac{Q_s}{\rho_s d}SSC \tag{3}$$

Where OBS is the optical backscatter signal $[V]$ and α_{OBS} is approximated as a constant for the range of SSC investigated.

Due to the dependency on $1/(\rho_s d)$, for the same concentration of sediment, the flux observed for $200\mu m$ sand ($\rho_s \approx 2600 kg/m^3$) will be 10 times smaller than for flocs of the same size ($\rho_{floc} \approx 1100 kg/m^3$), and even smaller in presence of microflocs.

1.3 Acoustic Backscatter Measurements

Analogously to OBS devices, an acoustic signal is emitted and backscattered by particles in suspension, then recorded by transducers. The estimation of SSC from acoustic measurements depends on the properties of sediment in suspension. For well-characterized particles (e.g., a well-sorted sand population) and electronically/acoustically calibrated sensors, backscattering models and representative diameters can be used to evaluate SSC from the theory [*Thorne and Hanes*, 2002]. Otherwise, similarly to optical sensors, the acoustic response can be calibrated against samples from field or laboratory experiments, with similar limitations regarding calibration representativity.

Acoustic devices typically used in coastal sediment studies can loosely be grouped into (i) single-frequency Acoustic Doppler Velocimeters (ADVs) which measure at a single point; (ii) single-frequency Acoustic Doppler Current Profilers (ADCPs) which measure over multiple points in the water column; and (iii) multi-frequency acoustic backscatter devices. Only the latter is specifically designed to measure suspended sediment concentration; ADCPs and ADVs were originally intended to measure velocity, but their operating principles mean that inferring sediment concentration from acoustic backscatter is a useful side benefit. In this study, we mainly consider acoustic backscatter from ADVs, which are widely used to measure suspended sediment concentrations [*Fugate and Friedrichs*, 2002; *Öztürk*, 2017; *Lin et al.*, 2020].

We can mathematically describe acoustic backscatter using the sonar equation, which balances the difference betweem energy emitted and received by the sensor with energy lost on the return trip of an acoustic pulse [*Hoitink and Hoekstra*, 2005]. The sonar equation is presented here in form similar to [*Hoitink and Hoekstra*, 2005; *Salehi and Strom*, 2011; *Chmiel et al.*, 2018]:

$$SNR = C - \underbrace{20\log_{10}(\psi R^2)}_{Spherical\ Spreading} - \underbrace{\int_0^R (\alpha_w(r) + \alpha_s(r))\,dr}_{Attenuation} + BI \tag{4}$$

SNR [dB] is the Signal-to-Noise Ratio recorded directly by the ADV, which indicates the intensity of acoustic backscatter. C [dB] is a constant including instrument-related and geometrical terms. The spherical spreading term ($20\log_{10}(\psi R^2)$) is a function of R [m], the one-way distance that the acoustic pulse travels from the transmitter to the measurement volume. The attenuation of the acoustic pulse can be decomposed into absorption by the water α_w [dB/m] and attenuation by sediment α_s [dB/m], integrated over the travel distance. BI is the volume backscatter strength [dB] and is a function of SSC and particle characteristics:

$$BI = 10\log_{10}\left(\frac{SSC\bar{\sigma}}{\rho_s \bar{V_s}}\right) \tag{5}$$

Where $\bar{\sigma}$ is the mean backscattering cross section [m^2], ρ_s is the dry particle density [kg/m^3], and $\bar{V_s}$ is the scattering volume [m^3].

The attenuation terms (α_s and α_w) are higher at larger concentrations and greater distances [*Thorne et al.*, 1993], but can be neglected below $1,000 mg/L$ [*Chmiel et al.*, 2018] and $O(10cm)$ from the sensor [*Pomázi and Baranya*, 2020]. In this study we thus neglect attenuation, given the small distance between source and measuring volume (15 cm) and low concentrations expected at our study site in Ameland ($< 1,000 mg/L$). All terms except BI can be reorganized and set in a global constant C' [dB]. Equation 5 then becomes:

$$SNR = 10\log_{10}(SSC) + 10\log_{10}\left(\frac{\bar{\sigma}}{\rho_s \bar{v_s}}\right) + C' \tag{6}$$

Equation 6 can be further simplified as:

$$SNR = 10\log_{10}(SSC) + b' + c' \tag{7}$$

where c' is a constant depending on instrument characteristics and b' is a variable depending on suspended particle properties (e.g., size, shape, density, elasticity). The log-linear relation between SNR and SSC is only valid for concentrations less than $1,000 mg/L$ [*Salehi and Strom*, 2011; *Chmiel et al.*, 2018]; beyond this threshold particle absorption losses reduce the recorded backscattering signal.

The interaction between an acoustic pulse and particles (scattering) is optimal for coarser individual (unflocculated) particles, with a dependency on the acoustic frequency such as $kD \approx d$ (or $< d$) where k is the wave number ($2\pi/\lambda$, and λ is the wavelength) and d the diameter of the particle [*Salehi and Strom*, 2011]. Hence for a $1Mhz$ acoustic signal, the optimal backscattering size (diameter) is around $480\mu m$, while for a $6Mhz$ signal, the optimal size is around $80\mu m$. Flocculated particles are characterized by lower backscattering efficiency (1 to 2 order of magnitude lower) [*Thorne and Hurther*, 2014]. Acoustic instruments are thus more sensitive to fine to coarse sands than fine flocculated particles [*Salehi and Strom*, 2011]: for similar concentrations, the SNR will be stronger for sand than for fine sediments.

1.4 Combining Optical and Acoustic Measurements: Towards the Sediment Composition Index (SCI)

In coastal and estuarine environments where suspended particles are often characterized by a mixture of fine sediments (including flocs) and sand particles, SSC measurements relying on a single technique (optical or acoustic) are ambiguous with respect to sediment composition. This can lead to misestimates of particle size and concentration [*Thorne et al.*, 2021], and limits the interpretability and representativeness of the recorded signal. The objective of the present paper is to combine the use of optical and acoustic backscatter sensors to estimate the relative fraction of sand in suspension.

Bass et al. [2007] note that although optical and acoustic backscatter systems are routinely used together, few studies have taken advantage of using them together to estimate suspended sediment composition in mixed environments. There is a salient difference in the response of optical and acoustic instruments to changes in suspended particle size [*Ha et al.*, 2009], which may be exploited to resolve ambiguities.

In some cases, it has been assumed that optical or acoustic instruments only observe a single class of sediment. *Bass et al.* [2002] disregard locally resuspended sand in their OBS measurements of fine sediment. In studies of tidal channels flanked by intertidal mud flats, both *Green et al.* [2000] and *van de Kreeke and Hibma* [2005] assumed that optical sensors detected only silt, while acoustic sensors detected only sand. The interpretation of a single instrument depends on the assumptions behind its calibration (e.g., an OBS calibrated to sandy sediment will overestimate total SSC when fine sediment is also present). However, instead of ignoring the presence of sand in optical measurements or the presence of fine sediment in acoustic measurements, paired instruments can more beneficially be used concurrently and compared [*Conner and De Visser*, 1992; *Green and Boon*, 1993; *Hawley*, 2004]. In this study, we take advantage of these paired instruments to derive a Sediment Composition Index (SCI) that quantitatively discriminates the presence of suspended sand from mud.

This relative optical-acoustic backscatter response can be analyzed by combining Equations 3 and 7 to obtain:

$$SNR = 10\log_{10}(OBS) + b_{particle} + c_{instr} \tag{8}$$

where $b_{particle}$ is a variable parameter function of SPM characteristics and c_{instr} is a global (optical/acoustic) instrument-related constant. In our study, as instruments were not calibrated, $b_{particle} + c_{instr}$ are considered as a single constant, the Sediment Composition Index (SCI). SCI is therefore dependent on the characteristics of the sediment particles being measured and of the instruments being used. Equation 8 can be rearranged to present SCI:

$$SCI = 10\log_{10}(OBS) - SNR \tag{9}$$

Considering the high sensitivity of the acoustic sensor to sand and of the optical sensor to fine sediments, SCI is relatively smaller when suspended sand particles dominate, and relatively larger when fine sediment dominates suspensions. SCI can thus be used as an indicator of sand or fine sediment dominance.

2 Methods

First, we use laboratory measurements as a proof of concept for the SCI, and to quantify the relationship between SCI and the fraction of sand in suspension (f_{sand}). The fraction of mud or fine sediment in suspension can also be directly calculated via $f_{mud} = 100\% - f_{sand}$. We then analyze *in situ* measurements to demonstrate the added value of SCI for investigating the dynamics of mixed-sediment environments. We compared optical/acoustic signals measured on Ameland ebb-tidal delta in the Netherlands (Figure 2), calculated SCI and f_{sand}, and put them into context with other simultaneous measurements (tidal stage) and derived parameters (bed shear stress due to waves and currents). By interpreting these measurements, we can test whether SCI is a valid and useful indicator of relative suspended sand or fine sediment dominance in estuarine environments.

2.1 Laboratory Experiments

We used the DEXMES (*Dispositif EXpérimental de quantification des Matières En Suspension*) tank for our experiments. DEXMES is operated by Ifremer and managed together with Géosciences Océan, Géosciences Rennes, and SHOM (French Hydrographic Service). The glass-walled tank has a volume of approximately $1m^3$ and internal diameter of $0.97m$ (Figure 1), and was filled with fresh water.

Two sets of similar experiments were conducted to evaluate SCI at various total sediment concentration ranges and sand/fine sediment contents. In Experiment 1, pure bentonite ($d_{50} < 63\mu m$) and two classes of well-sorted pure quartz sand ($\rho_s = 2,650 kg/m^3$) with median grain sizes $d_{50} \approx 100\mu m$ and $200\mu m$, were used to represent fine and coarse sediment, respectively. The $d_{50} \approx 100\mu m$ sand and $d_{50} \approx 200\mu m$ sands were additionally

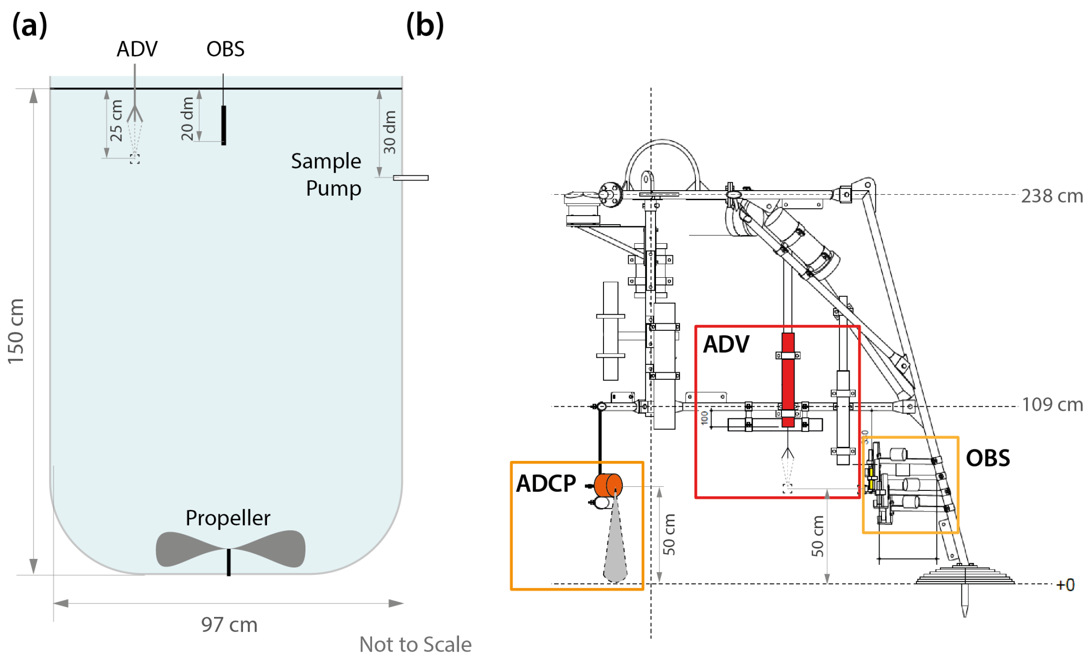

Figure 1. Overview of the DEXMES tank used in the laboratory experiments. (a) Schematic of instrument setup. During the experiments, the tank contained an Acoustic Doppler Velocimeter (ADV) and Optical Backscatter Sensor (OBS) mounted just below the surface. An external pump was connected to the tank to extract suspended sediment samples. (b) Frame used to conduct field measurements (AZG F4), featuring ADV, OBS, and downward-facing Acoustic Doppler Current Profiler (ADCP) sensors. The ADV and OBS measured sample volumes 50 cm above the base of the frame, and the ADCP measured a 50 cm profile between the instrument and the bed.

sieved with 100 to 125μm and 200 to 250μm meshes, respectively. Conversely, Experiment 2 used estuarine mud ($d_{50} < 63\mu m$) instead of bentonite, and the same sources of sand but without further sieving ($d_{50} = 93\mu m$ and $210\mu m$). For simplicity, we hereafter refer to $d_{50} \approx 100\mu m$ and $d_{50} \approx 200\mu m$ sand for both experiments.

Five sediment composition conditions were investigated for both 100 and 200μm sand in Experiment 1: pure fine sediment, pure sand, and 3 intermediate mixtures: 25%, 50% and 75% sand content (f_{sand}). For each condition, 6 total concentrations were tested stepwise from $15mg/l$ to $200mg/l$. In Experiment 2, fine sediment concentration was held constant at approximately $130mg/l$ and sand concentration incrementally varied between 0 and $1,460mg/l$, in order to approximate an estuarine environment with a sandy local bed composition and steady background presence of fine sediment (e.g., *Green et al.* [2000]; *van de Kreeke and Hibma* [2005]). Concentrations of both classes of sediment were kept within the linear range of response for each instrument ($< 5,000mg/L$ of fine sediment and $< 50,000mg/L$ of sand for the OBS [*Downing*, 2006] and $< 5,000mg/L$ for the ADV [*Salehi and Strom*, 2011]) to avoid ambiguity in the readings. Precise details of the suspended sediment concentrations and sand fractions in each experiment are provided in Supporting Information.

Vertical concentration gradients were observed within the tank for 200μm sand, but all instruments and samples measured within 10 cm of the same elevation, leading to comparable sample and sensor data. The propeller at the bottom of the tank was set to a speed of $175rpm$ to provide high turbulent shear between $G = 30$ and $100s^{-1}$, maximizing resuspension and mixture homogeneity while minimizing the formation of bubbles.

In Experiments 1 and 2, acoustic backscatter was measured using a Nortek Vector Acoustic Doppler Velocimeter [*Nortek AS*, 2005], operating at a frequency of 6 MHz, and sampling at 32 Hz (8 Hz in Experiment 2), 25 cm beneath the water surface. Optical backscatter was measured in Experiment 1 using a Wetlabs FLNTU *WET Labs Inc* [2019], sampling at 1 Hz, 20 cm beneath the water surface. In Experiment 2, a Campbell OBS 3+ [*Campbell Scientific Inc.*, 2014] was used instead, with similar properties to the Wetlabs FLNTU. To calibrate the optical and acoustic measurements, an external pump was connected to the tank 30 cm beneath the surface to extract suspended sediment samples. The instruments were arranged to avoid mutual interference but while sampling a similar elevation and hence similar sediment concentrations. All sensors were operated in continuous recording mode for the duration of each experiment, and statistics were computed over a 10-11 min period at each sediment concentration level. The median signal-to-noise ratio (SNR) of the three ADV beams and median OBS output were then used to calculate the relative optical-acoustic backscatter index *SCI* from Equation 9.

2.2 *In Situ* Measurements

Ameland Inlet is located in the Netherlands between the sandy barrier islands of Terschelling and Ameland, connecting the North Sea with the Dutch Wadden Sea (Figure 2). The inlet is characterized by a 30 m deep main channel (the “Borndiep") on its eastern side, and a shifting complex of shoals and channels on its west side. There is a large and highly dynamic ebb-tidal delta complex on the seaward side of the inlet, and a shallow backbarrier basin environment of intertidal shoals and flats on the landward side (the Wadden Sea) [*Elias et al.*, 2019; *Lenstra et al.*, 2019]. The seabed of the ebb-tidal delta of the inlet is mainly well-sorted fine sand (mean $d_{50} = 211\mu m$, $n = 165$) with with mud content generally $< 1\%$, whereas the Wadden Sea has a mud content up to 20% at its landward edge and on the intertidal flats separating Ameland Inlet from adjacent tidal basins [*Rijkswaterstaat*, 1999; *Pearson et al.*, 2019]. Samples with mud content of $\sim 5\%$ can also be found on the North Sea bed beyond the distal end of the ebb-tidal delta.

A field measurement campaign was carried out from August 29th to October 9th 2017, with the goal of characterizing hydrodynamic and sediment transport processes in the inlet and on its ebb-tidal delta [*De Wit et al.*, 2019; *Reniers et al.*, 2019; *Brakenhoff et al.*, 2019; *van der Werf et al.*, 2019; *van Prooijen et al.*, 2020]. Measurements of flow, waves, suspended particulate matter, bedform dynamics, and water quality were made at 4 locations across the site. Measurements considered in this study were obtained at frame AZG-F4 (Figure 2), at the distal end of the ebb-tidal delta, approximately 8m deep.

As with the laboratory experiments in Section 2.1, acoustic backscatter was measured using three Nortek Vector Acoustic Doppler Velocimeters (ADVs) [*Nortek AS*, 2005], operating at a frequency of 6 MHz, and sampling at 16 Hz, 20, 50, and 78 cm above the seabed. The median SNR of acoustic backscatter was taken over 30 minute bursts for the deployment period as per *Ha et al.* [2009].

Optical backscatter was measured using four Campbell OBS 3+ [*Campbell Scientific Inc.*, 2014], sampling at 16 Hz, 20, 30, 50, and 78 cm above the seabed. The OBS

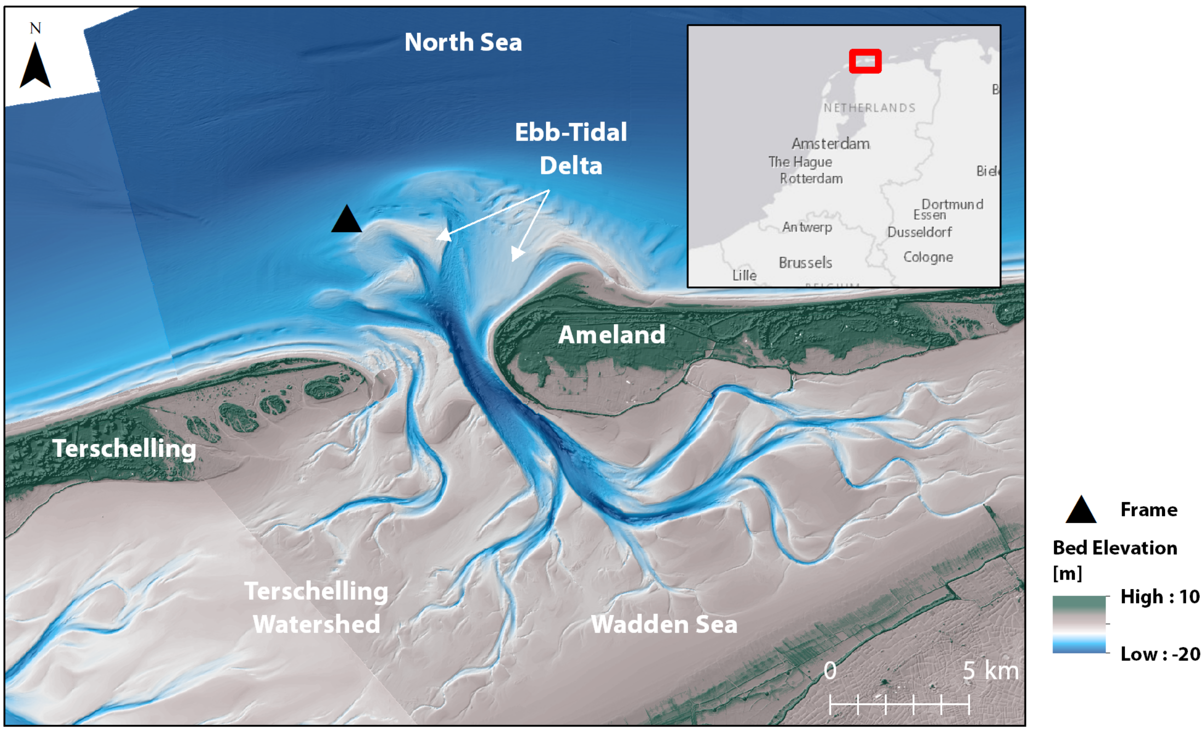

Figure 2. Overview of measurements during the September 2017 field measurement campaign at Ameland Inlet, including the frame (AZG-F4) bearing the instruments used in this study. The seabed sediment of the ebb-tidal delta consists predominantly of very fine sand (with mud content typically < 1%), whereas the intertidal flats of the Wadden Sea and Terschelling Watershed contain higher mud content [*Pearson et al.*, 2019]. Bathymetry source: Rijkswaterstaat Vaklodingen. Elevation source: Actueel Hoogtebestand Nederland (AHN), Rijkswaterstaat. Basemap sources: Esri, HERE, Garmin, ÂľOpenStreetMap contributors, and the GIS user community.

was initially calibrated using sandy sediment obtained from the seabed adjacent to the measurement frame. However, *Su et al.* [2016] note that using bed material to calibrate an OBS is “inappropriate" as doing so can introduce errors. On this basis, the calibration was discarded when it was recognized that the additional presence of suspended fine sediment in the field rendered it invalid. Thus, the uncalibrated OBS signal is presented here in volts. The median OBS signal over 30 minute bursts was used.

Near-bed hydrodynamic conditions during the monitoring period were measured using a high-resolution downward-looking Nortek Aquadopp Acoustic Doppler Current Profiler (ADCP-HR) [*Nortek AS*, 2008]. The ADCP sampled at a rate of 4 Hz in 30 minute bursts. These measurements were averaged over the water column between the sensor and the bed (approximately 0.5 m, depending on field conditions) and then median velocities were calculated for each 30 min burst interval. Bed shear stress due to the influence of waves and currents was calculated using the method of *Soulsby* [1997] (with default parameter settings) to give an indication of the potential for local bed material to be resuspended at the frame. For simplicity, we do not consider the effect of combined wave-current bed shear stresses here, which likely underestimates the frequency of sediment resuspension.

To assess the intratidal variation of the field measurements, we classified each 30 minute burst into flood tide, high water slack (HWS), ebb tide, and low water slack (LWS) based on an analysis of tidal currents [*Pearson et al.*, 2019]. At the measurement site, the major axis of flow is almost exactly in an east-west direction. Thus, eastward ($0 - 179$ deg) currents exceeding $0.1 m/s$ were classified as flood, and westward ($180 - 359$ deg) currents exceeding that threshold as ebb. Velocities below that threshold with positive water surface elevations (with respect to MWL) were classified as HWS, and with negative water surface elevations as LWS.

3 Results

3.1 Laboratory Experiments

3.1.1 Optical and Acoustic Backscatter

First, we consider the joint response of the optical and acoustic sensors to various sand/fine sediment mixtures: from purely fine suspensions to purely sand suspensions, and with varying total concentrations (Figure 3). Optical turbidity values are recorded in NTU or Volts (Experiment 1 and 2, respectively) depending on the instrument deployed. Readings in Volts are first normalized in equivalent NTU using an offset value in log space (constant for all Experiment 2 OBS data), so that their values are aligned in Experiments 1 and 2 for purely fine suspension conditions.

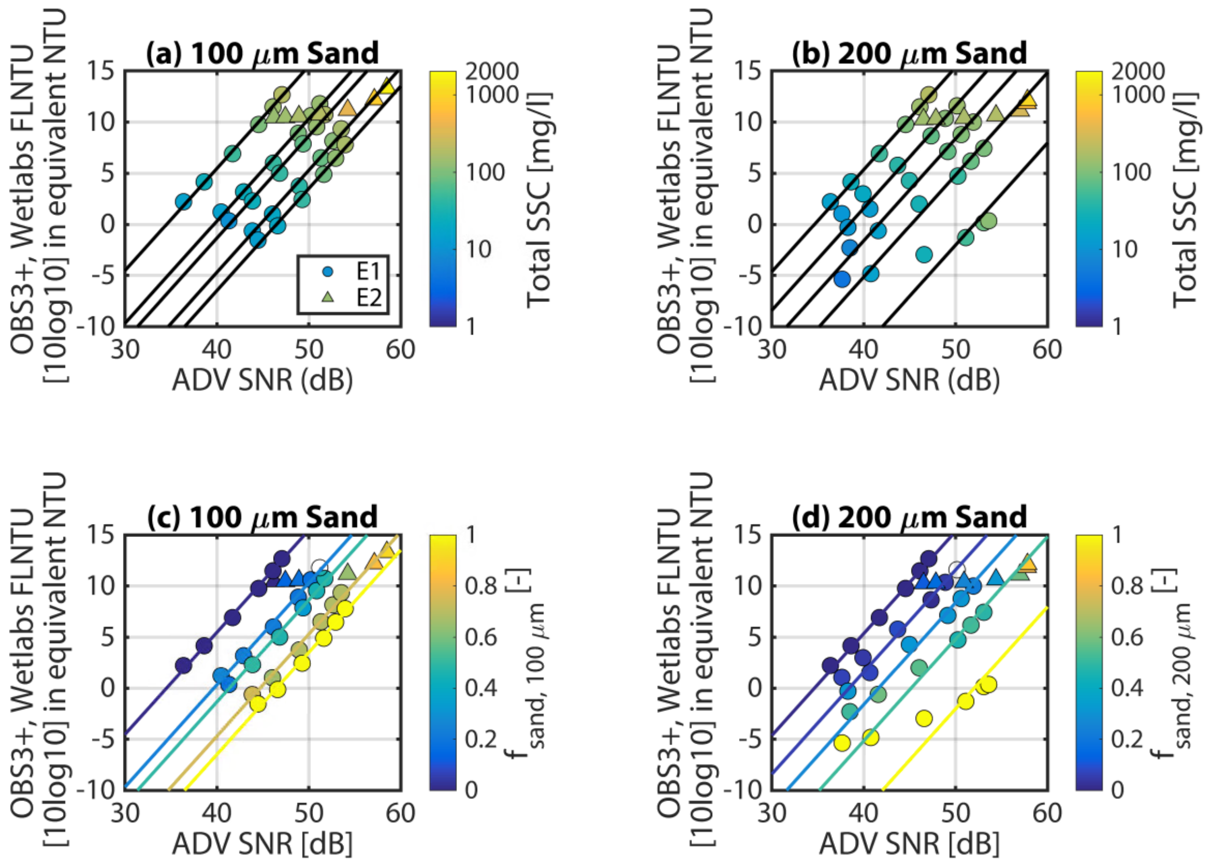

Figure 3. Median acoustic (ADV SNR) and optical backscatter (OBS) as a function of total suspended sediment concentration (a,b) and suspended sand fraction (f_{sand}) in the laboratory experiments (c,d). (a,c) Experiments with 100μm sand. (b,d) Experiments with 200μm sand. Data from Experiment 1 (E1) measured with a Wetlabs FLNTU, are marked with circles, while data from Experiment 2 (E2), measured with an OBS3+, are marked with triangles. Black and coloured lines indicate constant f_{sand} contours.

Results from Experiment 1 for 100μm sand (Figure 3a,c) show that the sensors' response is linear in $log_{10}(OBS)/ADVSNR$ space. This is valid for a range of total sediment concentration (from 15mg/l to 200mg/l), such that $10log_{10}(OBS) = SNR + SCI$, confirming the theoretical relationship (Equation 9). Increasing the sand fraction (f_{sand}) leads to a shift in the data alignment for the different conditions, but lines are still parallel

(Figure 3c). That is, for a given $ADVSNR$ value, the optical turbidity value increases as SPM becomes finer. Conversely, for a given optical turbidity value, $ADVSNR$ increases as SPM become sandier. Experiment 2 independently tested a larger total SSC gradient, increasing the sand content from 0 to 100% and total sediment concentration from $135mg/l$ to $1603mg/l$, while progressively adding sand (Figure 3a,c). These results are in full agreement with Experiment 1, with their data points matching the corresponding sand/fine sediment ratio contours as sand content increases.

Similar results are observed for $200\mu m$ sands: $log_{10}(OBS)/ADV$ pairs are aligned for a given sand content, and these lines are organized parallel to each other (Figure 3b,d). For similar turbidity values, the SNR signal is stronger for $200\mu m$ sand than for $100\mu m$ sand (Figure 3a,b). However, deviations from alignment are observed when sand content dominates (i.e., $f_{sand} > 50\%$) and total concentration is low (i.e., $SSC <= 50mg/l$). This bias corresponds to the poor sensitivity of the optical sensor to detect low $200\mu m$ particle concentrations, when there are few scatterers in suspension. In such conditions, recorded NTU values range from 0.1 to $0.9NTU$, close to the sensor resolution and lower detection limit. In order to include unbiased data in the analysis, turbidity data below $0.9NTU$ are discarded further in the study.

3.1.2 Sediment Composition Index (SCI)

We derived the sediment composition index SCI for the laboratory measurements using Equation 9, and it is shown to be an appropriate proxy for evaluating the sand content (Figure 4a). As a first step towards a generic SCI, we propose to normalize SCI such that $SCI = 0$ in purely fine sediment conditions.

To understand the relationship between the derived SCI and the actual sediment composition, we compare f_{sand} with SCI from both experiments and grain size classes, and find a negative correlation (Figure 4a). A hyperbolic tangent was fit to the data (Equation 10) because f_{sand} should asymptotically reach 0% for maximum SCI (minimum acoustic response, maximum optical response, no sand, only mud), and should tend asymptotically towards 100% for minimum SCI (maximum acoustic response, minimum optical response, only sand, no mud).

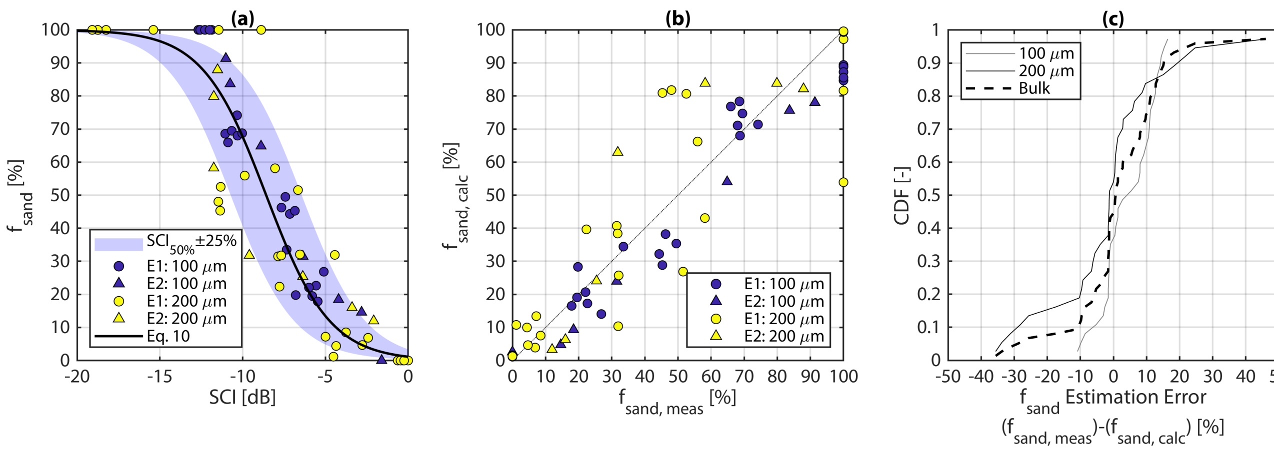

Figure 4. Fraction of sand in total suspended sediment (f_{sand}), calculated from the sediment composition index (SCI). (a) f_{sand} as a function of SCI, with Equation 10 fit to both grain sizes in bulk ($SCI_{50\%} = -8.58$). Blue bands indicate the envelope of uncertainty in f_{sand}, varying $SCI_{50\%}$ by ±25%. Experiments 1 and 2 (E1 and E2, respectively) are indicated, along with the sand grain size used in each experiment ($R^2_{100} = 0.957$; $R^2_{200} = 0.806$; $R^2_{bulk} = 0.884$). (b) Comparison of experimentally measured $f_{sand,meas}$ with $f_{sand,calc}$ determined using Equation 10. (c) Cumulative distribution function (CDF) of sand fraction estimation error ($f_{sand,meas} - f_{sand,calc}$) for each sand grain size class and for all classes combined in bulk.

$$f_{sand} = \left(\frac{1}{2} + \frac{1}{2}\tanh\left[\frac{(SCI - SCI_{50\%})}{\Delta SCI}\right]\right) \cdot 100\% \quad (10)$$

Where $SCI_{50\%}$ is a constant corresponding to a mixture of 50% sand and 50% mud. It is equal to -8.03 when fitting only $100\mu m$ sand ($R^2_{100\mu m}$ = 0.954), -9.63 for $200\mu m$ sand ($R^2_{200\mu m}$ = 0.848), and -8.58 when both grain sizes are fit in bulk (R^2_{bulk} = 0.884). For the analyses in the rest of this study, we consider $SCI_{50\%} = -8.58$. $\Delta SCI = 3.85$, and indicates the width in variation. Equation 10 allows us to deepen the interpretation of SCI by directly predicting f_{sand} (and by extension, $f_{mud} = 1 - f_{sand}$). It shows good predictive skill when compared with measured f_{sand} for both experiments and grain size classes (R^2_{100} = 0.957; R^2_{200} = 0.806; R^2_{bulk} = 0.884) (Figure 4b). The bulk prediction is accurate for $200\mu m$ sands, as 70% of the calculated sand fractions are associated with an absolute error lower than ±10%. Results are the best for the finest sand distribution ($100\mu m$), with more than 85% of the samples estimated with an absolute error below ±10%. In case the sand distribution is not known, we also investigated the SCI response to sand content when merging all experimental data (Figure 4c). This bulk index still performs well, with 70% of the calculations with errors within ±10%, although the error range is slightly larger, between −30% and +20%.

The clear relationships found in these lab experiments between optical and acoustic backscatter and varying sand content are captured in a single parameter by the SCI. These results confirm that SCI is a relevant proxy for describing the suspended particle composition, and can be used to directly estimate the fraction of sand in suspension (f_{sand}).

3.2 In Situ Measurements

After demonstrating that variations in sediment composition index (SCI) can accurately distinguish relative sand content in controlled laboratory experiments, we evaluated this index using field measurements from Ameland ebb-tidal delta [*van Prooijen et al.*, 2020].

3.2.1 Hydrodynamic Conditions

The measurements from Ameland ebb-tidal delta span 40 days (August 29 to October 8, 2017), or approximately 2.5 spring-neap cycles (Figure 5a). There are two minor storms ($H_s \approx 1m$) on August 30th and September 7th, and two major storms ($H_s > 4m$), *Sebastian* (September 14th, during neap tide) and *Xavier* (October 6th, during spring tide).

Spring tide occurs around September 10th, 20th, and October 7th (corresponding to the larger tidal range in Figure 5a). Under calmer conditions, bed shear stresses due to currents ($\tau_{b,c}$) exceed the critical threshold for local sand ($\tau_{cr,211\mu m} = 0.18Pa$) only during spring flood tides (Figure 5c and Figure 6f). These periods with currents strong enough to resuspend or advect sand correspond to flood and ebb stages of the tidal cycle (Figure 5a and Figure 6b).

Wave-induced bed shear stress $\tau_{b,w}$ is greatest during the storms (Figure 5b and Figure 6c), exceeding $\tau_{cr,211\mu m}$. High bed shear stresses due to currents ($\tau_{b,c}$) are also observed during the two major storms, likely due to wind-induced storm surge and wave-driven currents (Figure 5b). During *Storm Sebastian* on September 14th, eastward currents during the peak of the storm were so strong and persistent that the tide did not reverse (no ebb occurred for nearly 24 hours). During storm periods, $\tau_{b,w}$ is greatest at low tide.

3.2.2 Optical and Acoustic Backscatter

Over the total deployment period, OBS measurements show strong tidal variation and a response to individual storm events (Figure 5d and Figure 6h). The largest ADV readings occur during spring tide and the peaks of the two largest storms (Figure 5e and Figure 6i,j), while the lowest ADV SNR readings tend to correspond to calmer periods with low wave stress (Figure 5e and Figure 6j).

During Storm Sebastian on September 12th-16th, both SNR and OBS signals strongly increase and tidal variation is weak for the next 2 tidal cycles (Figure 6g,i). Both signals remain relatively high but noisy, and higher background (minimum) readings persist for about a week after the storm.

During the calm spring tidal period from September 21st-25th, the influence of waves is minimal and the intratidal dynamics are clear (Figure 6h,j). The OBS signal shows strong M2 (semi-diurnal) tidal oscillations peaking around low water slack. Conversely, ADV SNR shows mixed M2 and M4 (quarter-diurnal) tidal variation, peaking at flood tide and to a lesser degree at ebb. ADV SNR is lowest at high water slack. The calm period from September 28th to October 2nd coincides with neap tide and exhibits

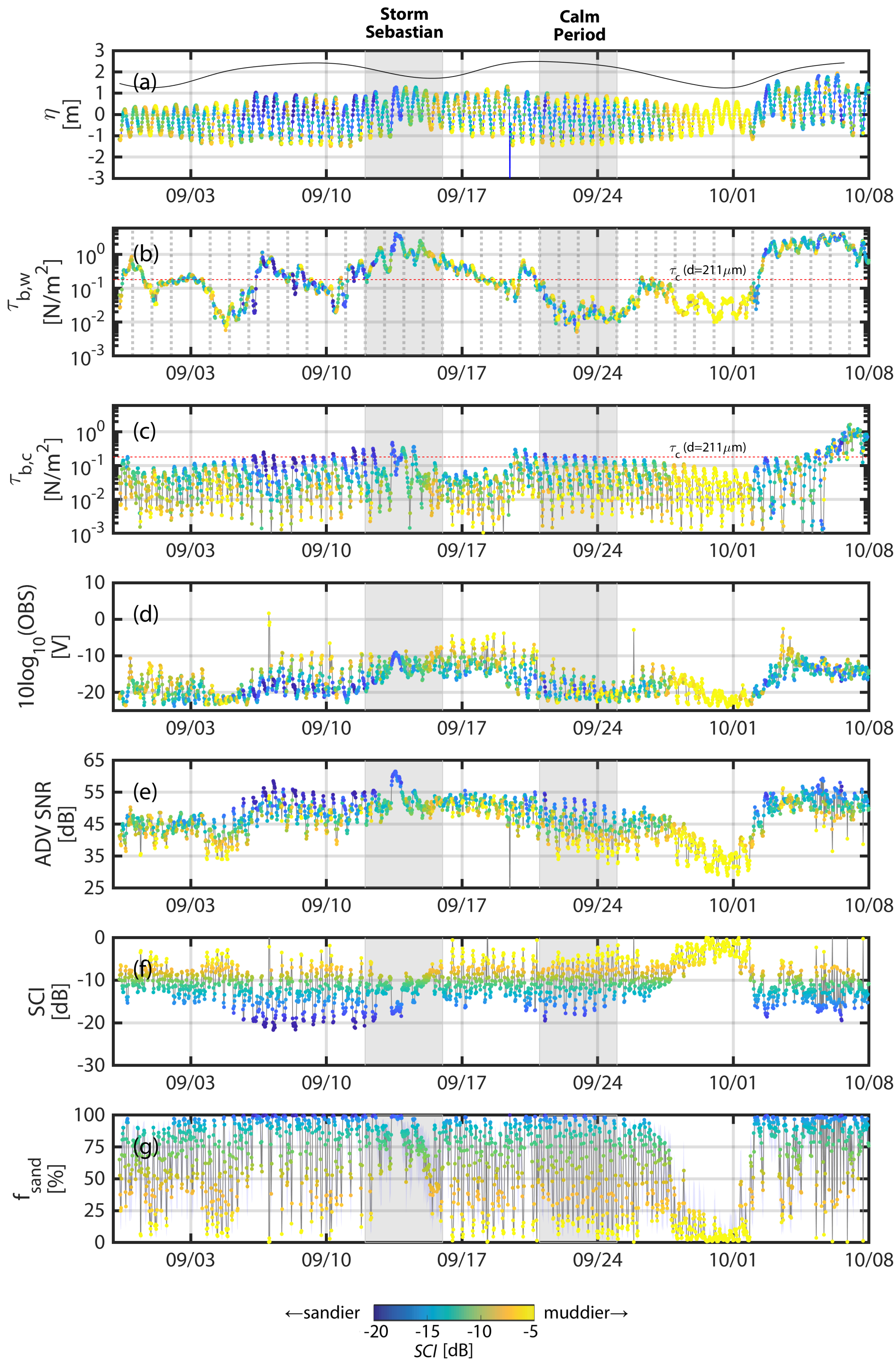

Figure 5. Time series of hydrodynamic conditions and backscatter at Ameland ebb-tidal delta Frame 4, with dot colour indicating relative optical-acoustic backscatter index *SCI*. Higher *SCI* (lighter yellow colours) suggest relatively higher fine sediment content, and lower *SCI* (darker blue colours) suggest relatively higher sand content. (a) Water level relative to the mean depth during the deployment period (8.3*m*). The tidal range (indicated with a solid black line) shows spring tide (high values) and neap tide (low values).

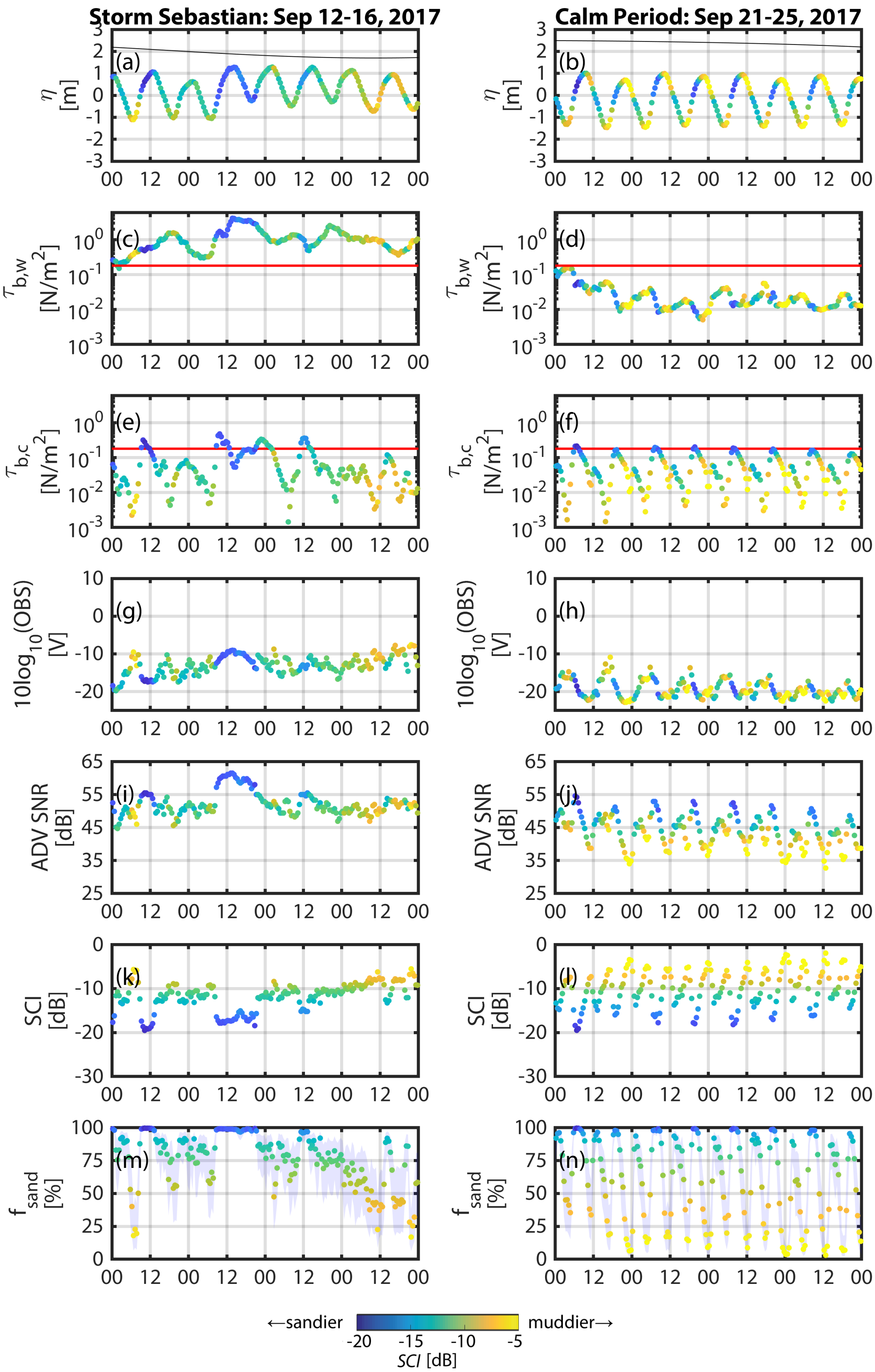

Figure 6. Time series of hydrodynamic conditions and backscatter at Ameland ebb-tidal delta Frame 4, focusing on Storm Sebastian (Sept 12-16) and a calmer period during spring tide (Sept 21-25). Dot colour indicates relative optical-acoustic backscatter index *SCI*. Higher *SCI* (lighter yellow colours) suggest relatively higher fine sediment content, and lower *SCI* (darker blue colours) suggest relatively higher sand content. (a,b) Water level (η) relative to the mean depth during the deployment period (8.3m). The tidal range (indicated

similar dynamics to the pre-storm period at the beginning of the monitoring period, albeit with lower background OBS and ADV SNR levels and reduced intratidal variability.

3.2.3 Sediment Composition Index (SCI) and f_{sand}

From the optical and acoustic backscatter readings, we could then estimate the suspended sediment composition. We calculated SCI with Equation 9, using the OBS and ADV SNR measurements 50 cm above the bed. SCI was offset to zero by subtracting its 99^{th} percentile value. As in the laboratory experiments, this corresponds to a condition when sand is not likely present. This assumption is corroborated by the calm hydrodynamic conditions during moments of high SCI. We then applied Equation 10 with $SCI_{50\%} = -8.58$ (fit to both 100 and 200μm sand) to the SCI time series including the confidence bands to approximate the fraction of sand in suspension (f_{sand}).

At subtidal timescales, SCI is lower during storms and spring tides (e.g., Figure 6k,l). SCI reaches its lowest observed values during spring tide, during both calm and stormy periods (Figure 5b). By contrast, it is highest during calm conditions and neap tide (e.g., Figure 5f from Sep 28 to Oct 2). SCI is much more dynamic at spring tide, its standard deviation nearly doubling when compared to neap tide.

Over the course of a tidal cycle, SCI typically follows a mixed M2 and M4 pattern. The M4 signal has minima at flood and ebb tide, and is especially pronounced during spring tidal conditions. Superimposed on this is an M2 variation with its peak centred at ebb tide. The combination of these two signals results in minimal SCI at flood tide when $\tau_{b,c}$ is high, then a peak at high water slack when $\tau_{b,c}$ is low (Figure 6l). This is followed by a sharp drop to a secondary minimum at ebb tide (when $\tau_{b,c}$ increases again), and then a gradual rise to another peak at low water slack. The cycle completes with another rapid decline in SCI at flood tide as currents strengthen. Although SCI nearly always peaks at slack water, the maximum varies between low water slack (e.g., Sep 8-10) and high water slack (e.g., Sep 21-25).

SPM is dominated by sand at ebb and flood tide, when $f_{sand} > 75\%$ (Figure 6n). Conversely, the suspension consists primarily of fine sediment at high and low water slack ($f_{sand} < 25\%$). f_{sand} follows an M4 signal, with only weak M2 variations compared to SCI.

The presence of waves (indicated by higher wave-induced bed shear stress $\tau_{b,w}$) is often associated with lower SCI (Figure 5b). During Storm Sebastian on September 13th, SCI drops during the peak in the storm, and loses its characteristic M2-M4 tidal variation for several days (Figure 6k). This corresponds to a period of mainly sand in suspension (f_{sand} > 75%), with f_{sand} approaching 100% at the peak of the storm (Figure 6m). The proportion of fine sediment in suspension increases towards the end of the storm, and tidal variations in f_{sand} begin to return.

To further explore the influence of waves on tidal variations in relative optical-acoustic response, we plot SCI as a function of wave ($\tau_{b,w}$) and current-related bed shear stresses ($\tau_{b,c}$) at each stage of the tidal cycle (Figure 7). We summarize the variability of SCI relative to wave and current forcings (shear stresses), separating results into flood and ebb tidal phases. In this shear stress space, the dynamics of SCI are clearly structured.

During calm flood tides ($\tau_{b,w} < \tau_{cr,211\mu m}$), SCI ranges from $0dB$ during weak currents to $-22dB$ during stronger currents. A similar pattern is observed during ebb, although generally $SCI > -15dB$. This can be explained by the weaker $\tau_{b,c}$ during maximum ebb compared with during maximum flood. Both high and low water slack are characterized by relatively high SCI ($> -10dB$). SCI reaches $< -12dB$ during slack periods during wavy conditions. Larger wave-induced stresses are generally associated with $SCI < -5dB$, although brief peaks in SCI can sometimes be observed during storms (Figure 5).

4 Discussion

4.1 Interpreting the Dynamics of the Sediment Composition Index (SCI)

The sediment composition index (SCI) is a useful indicator of the relative fractions of sand and fine sediment in suspension, as validated in laboratory experiments. We further demonstrate the application of this index by interpreting the sediment dynamics on Ameland ebb-tidal delta in light of two main processes: resuspension of local sandy bed material by waves and strong tides, and tidal advection of fine sediment from locations outside the ebb-tidal delta. These processes explain the response of optical and acoustic backscatter measurements, and hence the corresponding dynamics of SCI.

At subtidal timescales (> 24 hours), the dynamics of SCI can be explained in part by a fortnightly spring-neap cycle. The larger intratidal variation of SCI at spring tide is

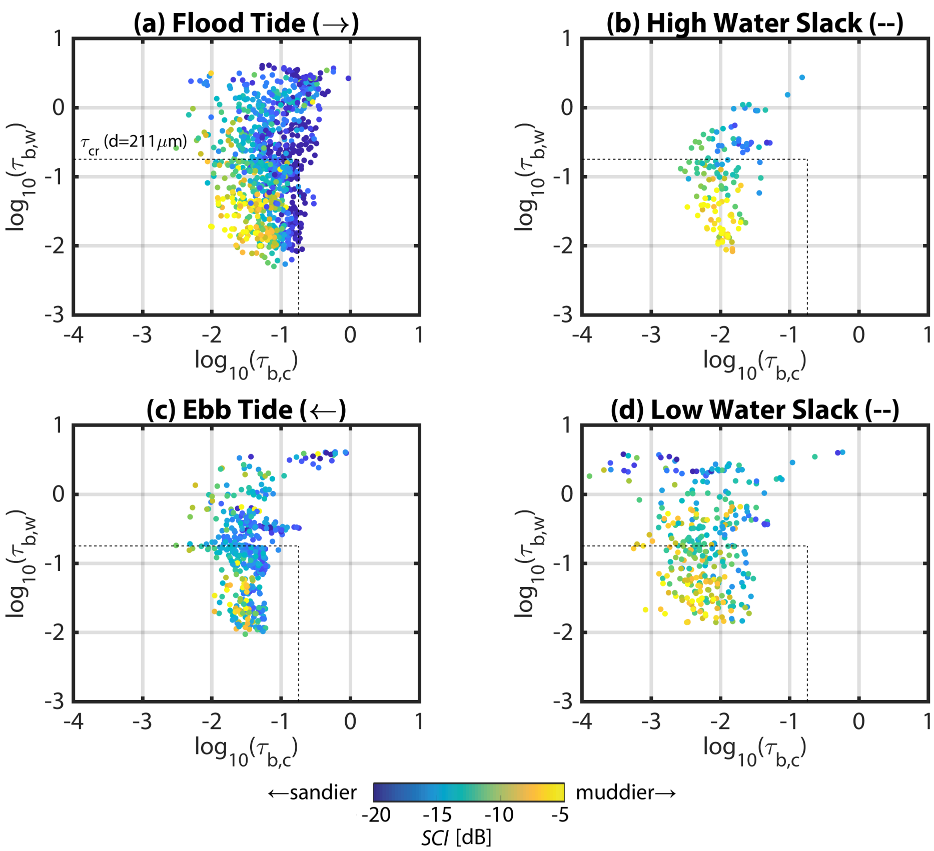

Figure 7. Sediment composition index *SCI* (in color) as a function of wave shear stress (vertical axes) and current shear stress (horizontal axes), at four different stages of the tidal cycle. (a) Flood tide ($u > 0.1m/s$ and to the east); (b) high water slack ($u < 0.1m/s$ and at high water); (c) ebb tide ($u > 0.1m/s$ and to the west); (d) low water slack ($u < 0.1m/s$ and at low water). The critical shear stress for local $211\mu m$ sand ($0.18Pa$) is plotted for reference as a dotted line. Bed shear stresses were computed using *Soulsby* [1997].

likely due to the increased resuspension of sand by stronger currents (Figure 5c) and to the greater advection of fine sediment from nearby intertidal flats at late ebb and LWS, similarly to the observations of *Weeks et al.* [1993] and *Fettweis et al.* [1998] at other sites. Conversely, high SCI (and thus higher relative proportions of fine sediment in suspension) coincides with the neap tide (e.g., Sep 28-Oct 1) and with lower values of $\tau_{b,w}$ and $\tau_{b,c}$. Without sufficiently strong forcing to resuspend local sand (Figure 5c), only fine sediment can remain in suspension.

The observed intratidal variation in SCI (Figure 6l) can be explained by the local hydrodynamics and sedimentary environment, and is summarized conceptually in Figure 8. At flood and ebb tide, strong currents are capable of resuspending sand from the local seabed or advecting it from elsewhere nearby, so the corresponding SCI values decrease. Conversely, when sand settles out at slack water, only the suspended fine sediment remains in the water column, explaining the increase in SCI value at that time. The result is an M4 signal with minima at flood and ebb tide. This relationship between local resuspension and local current velocities is also observed by [*Lavelle et al.*, 1984; *Weeks et al.*, 1993; *Bass et al.*, 2002; *van de Kreeke and Hibma*, 2005].

Modulating the M4 SCI signal is an M2 signal with its maximum centred at ebb tide. This M2 signal can be explained by the semidiurnal migration of a strong landward fine sediment concentration gradient in the channels of Ameland basin [*Postma*, 1961]. Remote sensing indicates that this turbid water mass can be ejected several kilometres seaward of the inlet and across the ebb-tidal delta at ebb [*Pearson et al.*, 2019], which causes the corresponding SCI to increase. This muddy water mass is then displaced by less turbid oceanic water on the flood tide, so SCI decreases again. This semidiurnal transport pattern is widely observed at other sites where there is a persistent gradient in suspended fine sediment concentration [*Weeks et al.*, 1993; *Green et al.*, 2000; *Bass et al.*, 2002; *van de Kreeke and Hibma*, 2005].

To fully explain the SCI dynamics at Ameland, the episodic influence of storms must also be accounted for. If waves are sufficiently large ($\tau_{b,w} > \tau_{cr,211\mu m}$), then the majority of local sand can be mobilized, which can result in low values of SCI regardless of the tidal stage. Conversely, the periods with the lowest SCI (suggesting lower proportions of sand in suspension and relatively more fine sediment) coincide mainly with periods of low wave action (e.g., Sep 28-Oct 1).

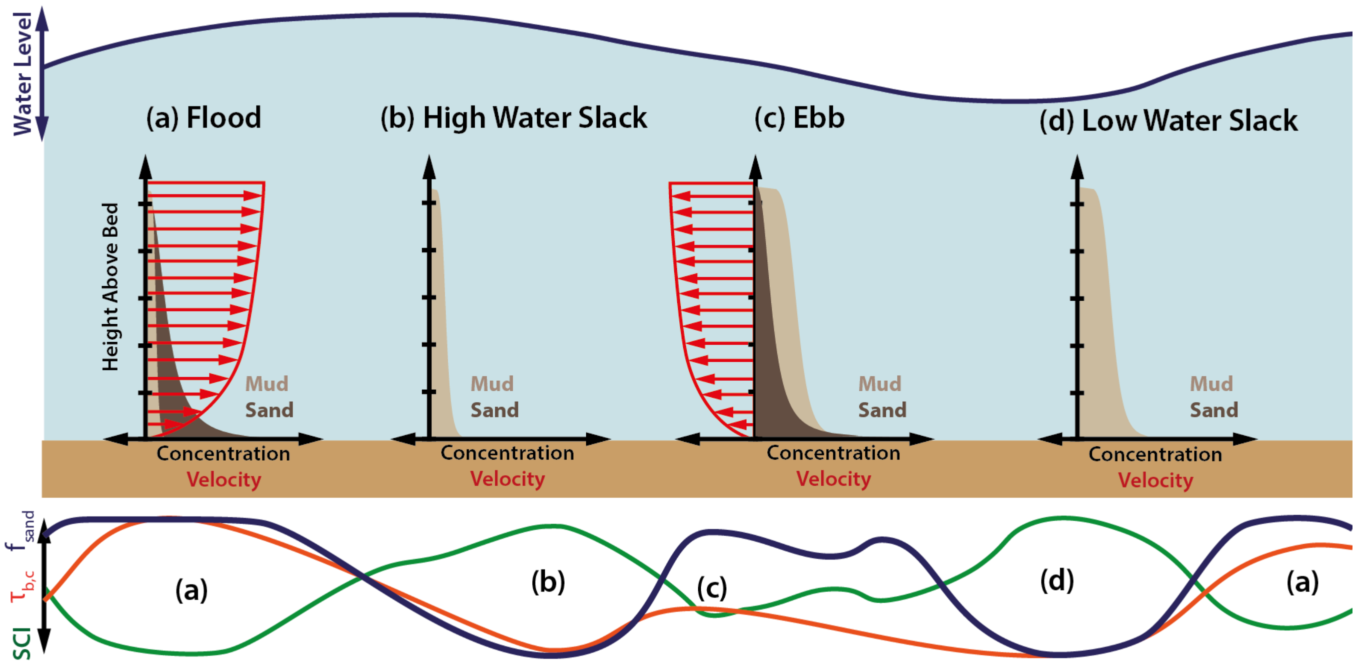

Figure 8. Conceptual model of tidally-driven mixed sand-fine sediment transport at the study site on Ameland ebb-tidal delta. A normalized example time series of sediment composition index (SCI), bed shear stress due to currents ($\tau_{b,c}$), and fraction of sand in suspension (f_{sand}) over a tidal cycle are indicated below. (a) At flood tide, strong currents locally resuspend sand, but carry few fine particles from the North Sea, so SCI is low. (b) At high water slack, currents are too weak to mobilize sand, so total concentrations are relatively low and consist only of fines, so SCI is higher. (c) At ebb tide, strong currents locally resuspend sand, though less than at flood tide, so SCI decreases again. These ebb currents also carry with them fine particles from the muddy and biologically productive Wadden Sea. (d) At low water slack, currents are too weak to mobilize sand, leaving only the fine material advected from the Wadden Sea at ebb, which begins to settle, resulting in higher SCI.

During periods with large waves, SCI may be influenced not just by an increased capacity for local resuspension of sand, but also by wind and wave-induced fine sediment resuspension. This is reflected in the SCI signal during Storm Sebastian (Figure 6). Even when bed shear stresses due to waves and currents greatly exceed $\tau_{cr,211\mu m}$, SCI seldom drops below $-15dB$ and f_{sand} remains between $50-90\%$ for most of the storm. In the latter half of the storm, f_{sand} decreases as sand settles out, while fine sediment remains in suspension. This fine material can originate from two locations: the Wadden Sea tidal basin or the bed of the North Sea. During storms, tidal flats in Ameland basin may easily lose the surface layers of sediment deposited in calm periods [*Postma*, 1961]. In a similar case study, *Green et al.* [2000] found that wave activity on nearby intertidal flats was the principal determinant of suspended fine sediment load advected through a tidal channel. However, storms may also remobilize fine sediment which accumulates in the bed of the North Sea [*van der Hout et al.*, 2017; *Flores et al.*, 2017; *Hendriks et al.*, 2020]. Instantaneous bed shear stress does not tell the whole story of suspended sediment composition: it is also necessary to account for spatial and temporal variations in the supply of fine sediment.

Our interpretation of SCI based on theoretical considerations and the laboratory results are fully supported by the local hydrodynamics and sedimentological context. SCI thus provides a novel and valuable characterization of the suspended sediment dynamics on Ameland ebb-tidal delta. This metric is especially useful for mixed-sediment environments like Ameland where optical and acoustic measurements are otherwise ambiguous when viewed in isolation.

4.2 Limitations & Outlook

Having been conceptually validated by laboratory and field measurements, there are many opportunities for further developing the SCI and improving its applicability. The next steps towards a more quantitative evaluation of sediment composition lie in the accumulation of larger datasets and in quantifying the component of SCI specific to the instruments being used (the c_{instr} term of Equation 8, which is invariant with SPM).

For a more generic SCI, we propose a reference calibration of optical and acoustic sensors to evaluate the instrument constant c_{instr} (Equation 8), using NTU/BTU (formazin calibration) for optical systems, and monodispersed glass beads for acoustic particles, similarly to the calibration procedure for an ABS system (e.g., *Thorne and Meral* [2008]). With calibrated scatterers, the sonar equation (Equation 4) can be fully evaluated, the instrument constant c_{instr} is the only unknown. Acoustic backscatter is sensitive to the acoustic frequency of the transducers: the SCI dynamics will be different from 1 MHz to 6 MHz sensors, because each sensor will respond differently to sediment of a given grain size and concentration. Similarly, optical sensors will provide different NTU values depending on whether the optical sensor is based on backscatter (e.g., OBS 3+ [*Campbell Scientific Inc.*, 2014], Seapoint *Seapoint Sensors Incorporated* [2013], or Wetlabs [*WET-Labs*, 2010]) or sidescattering (e.g., YSI 6600 [*YSI Incorporated*, 2012]). Many additional laboratory experiments would be required in order to determine c_{instr} and make a full set of conversion factors for each type of instrument. By applying these calibrations, SCI could become generic, at least for similar instruments. However, even without quantifying c_{instr} directly, SCI provides useful information on suspended sediment composition when its dynamics are considered in the context of local hydrodynamic and sedimentological conditions.

Additional laboratory experiments must be carried out with a wider variety of sediment mixtures and concentrations. We expect that most of the variability of SCI is caused to first order by the presence of sand in suspension, because sand has a relatively stronger influence on acoustic backscatter than flocs of comparable size [*Thorne and Hurther*, 2014]. However, the influence of flocculation on the variability of SCI requires further investigation.

Field measurements should also be collected from sites with different sedimentary characteristics under a range of hydrodynamic conditions in order to generalize the conclusions of the present study and $SCI{-}f_{sand}$ relationships like Equation 10. Samples pumped at regular intervals (e.g., *Beamsley et al.* [2001]) or better yet, at moments triggered by specific turbidity levels, would provide a more representative basis for calibrating optical and acoustic measurements. Fortunately, analyzing SCI dynamics of additional field sites is already possible, since optical and acoustic instruments are frequently paired together in the field (e.g.,*Fugate and Friedrichs* [2002]; *Voulgaris and Meyers* [2004]; *Moura et al.* [2011]; *Flores et al.* [2018]; *Zhu et al.* [2019]; *Lin et al.* [2020]; *de Vet et al.* [2020]; *Colosimo et al.* [2020]; *Pomeroy et al.* [2021]). Our approach thus gives added value to existing datasets by providing an additional, simple-to-calculate metric for interpreting sediment dynamics.

These additional efforts to make SCI more general and to better understand the underlying physics will strengthen the usefulness and applicability of the metric. This will lead to new insights into the dynamics of mixed sediment environments where ambiguity due to suspended sediment composition previously limited the information that could be obtained from optical and acoustic measurements.

5 Conclusions

The sediment composition index (SCI) derived in this study quantifies the suspended sediment composition in mixed-sediment environments. It does so using the relative intensity of optical and acoustic backscatter signals, as these two measurement techniques have different sensitivities to sand and fine sediment (Equation 9). SCI can be used to estimate the fraction of sand and fine sediment in suspension (f_{sand} and f_{mud}) in marine environments. Here, we verify the theoretical response of these optical and acoustic instruments in laboratory experiments. SCI is negatively correlated with the fraction of sand in suspension (Equation 10).

We successfully applied this approach to *in situ* measurements on the ebb-tidal delta of Ameland Inlet in the Netherlands. SCI shows a clear M4 variation associated with suspension of local sand, modulated by an M2 variation associated with suspended fine sediment advected from the nearby Wadden Sea. Lower values of SCI (indicating a stronger acoustic response) and higher f_{sand} are observed under more energetic conditions when sand is expected to dominate the suspension (e.g., spring flood tide or strong wave conditions). Conversely, SCI increases (indicating a stronger optical response) and f_{sand} reduces in calmer conditions and at slack water, when the suspended sediment consists mainly of fine sediment.

This approach reduces the ambiguity of suspended sediment composition in mixed sediment environments. Furthermore, it adds value to existing sets of measurements since simultaneous optical/acoustic measurements have frequently been carried out together in sediment transport studies. Being able to discern between different types of sediment in suspension will increase confidence in the interpretation of suspended sediment concentration measurements. This can ultimately improve estimates of sediment fluxes, leading to deeper understanding of coastal systems and enable better-informed coastal management decision-making.

Acknowledgments

This work is part of the research programme âĂŸCollaboration Program WaterâĂŹ with project number 14489 (SEAWAD), which is (partly) financed by NWO Domain Applied and Engineering Sciences. SGP was partly funded by ISblue within their Foreign Student Mobility Programme. Special thanks to the Dutch Ministry of Infrastructure and Water Management (Rijkswaterstaat and Rijksrederij) for their ongoing support as part of the Kustgenese2.0 project. Data archiving for this study is currently underway, with some data already publicly available at 4TU Centre for Research Data at https://doi.org/10.4121/collection:seawad *Delft University of Technology et al.* [2019]. Details of this dataset can be found in *van Prooijen et al.* [2020] and *van der Werf et al.* [2019]. Additional data files have been temporarily included here as supporting information for the review process:

`https://surfdrive.surf.nl/files/index.php/s/q1slh1EqhRkUhl1`

References

Bass, S. J., J. N. Aldridge, I. N. McCave, and C. E. Vincent (2002), Phase relationships between fine sediment suspensions and tidal currents in coastal seas, *Journal of Geophysical Research: Oceans*, *107*(10), 1–14, doi:10.1029/2001jc001269.

Bass, S. J., I. N. McCave, J. M. Rees, and C. E. Vincent (2007), Sand and mud flux estimates using acoustic and optical backscatter sensors: Measurements seaward of the Wash, southern North Sea, *Geological Society Special Publication*, *274*, 25–35, doi:10.1144/GSL.SP.2007.274.01.04.

Beamsley, B. J., K. P. Black, and T. Healy (2001), Micro-scale Pumped Measurements of Suspended Sediment Over a Mixed Sand/Mud Bed: Profiles, Grain Sizes and Sediment Diffusivity, *Journal of Coastal Research*, (34), 342–356.

Brakenhoff, L., M. Kleinhans, G. Ruessink, and M. Vegt (2019), Spatio?temporal characteristics of small?scale wave?current ripples on the Ameland ebb?tidal delta, *Earth Surface Processes and Landforms*, doi:10.1002/esp.4802.

Campbell Scientific Inc. (2014), OBS-3+ and OBS300 Suspended Solids and Turbidity Monitors, *Tech. rep.*, Campbell Scientific Inc., Logan, utah.

Chapalain, M., R. Verney, M. Fettweis, M. Jacquet, D. Le Berre, and P. Le Hir (2019), Investigating suspended particulate matter in coastal waters using the fractal theory, *Ocean Dynamics*, *69*(1), 59–81, doi:10.1007/s10236-018-1229-6.

Chmiel, O., I. Baselt, and A. Malcherek (2018), Applicability of Acoustic Concentration Measurements in Suspensions of Artificial and Natural Sediments Using an Acoustic Doppler Velocimeter, *Acoustics*, *1*(1), 59–77, doi:10.3390/acoustics1010006.

Colosimo, I., P. L. de Vet, D. S. van Maren, A. J. Reniers, J. C. Winterwerp, and B. C. van Prooijen (2020), The impact of wind on flow and sediment transport over intertidal flats, *Journal of Marine Science and Engineering*, *8*(11), 1–26, doi: 10.3390/jmse8110910.

Conner, C. S., and A. M. De Visser (1992), A laboratory investigation of particle size effects on an optical backscatterance sensor, *Marine Geology*, *108*(2), 151–159, doi: 10.1016/0025-3227(92)90169-I.

de Vet, P. L., B. C. van Prooijen, I. Colosimo, N. Steiner, T. Ysebaert, P. M. Herman, and Z. B. Wang (2020), Variations in storm-induced bed level dynamics across intertidal flats, *Scientific Reports*, *10*(1), 1–15, doi:10.1038/s41598-020-69444-7.

De Wit, F., M. Tissier, and A. J. Reniers (2019), Characterizing wave shape evolution on an ebb-tidal shoal, *Journal of Marine Science and Engineering*, *7*(10), 1–20, doi: 10.3390/jmse7100367.

Delft University of Technology, Utrecht University, and University of Twente (2019), *SEA-WAD: SEdiment supply At the WAdden Sea ebb-tidal Delta*, 4TU.Centre for Research Data, doi:10.4121/collection:seawad.

Downing, J. (2006), Twenty-five years with OBS sensors: The good, the bad, and the ugly, *Continental Shelf Research*, *26*(17-18), 2299–2318, doi:10.1016/j.csr.2006.07.018.

Elias, E. P., A. J. F. Van Der Spek, S. G. Pearson, and J. Cleveringa (2019), Understanding sediment bypassing processes through analysis of high- frequency observations of Ameland Inlet , the Netherlands, *Marine Geology*, *415*(May), 105,956, doi: 10.1016/j.margeo.2019.06.001.

Fettweis, M., M. Sas, and J. Monbaliu (1998), Seasonal, neap-spring and tidal variation of cohesive sediment concentration in the Scheldt Estuary, Belgium, *Estuarine, Coastal and Shelf Science*, *47*(1), 21–36, doi:10.1006/ecss.1998.0338.

Fettweis, M., R. Riethmüller, R. Verney, M. Becker, J. Backers, M. Baeye, M. Chapalain, S. Claeys, J. Claus, T. Cox, J. Deloffre, D. Depreiter, F. Druine, G. Flöser, S. Grünler, F. Jourdin, R. Lafite, J. Nauw, B. Nechad, R. Röttgers, A. Sottolichio, T. V. Engeland, W. Vanhaverbeke, H. Vereecken, T. Van Engeland, W. Vanhaverbeke, and H. Vereecken (2019), Uncertainties associated with in situ high-frequency long-term observations of suspended particulate matter concentration using optical and acoustic sensors, *Progress in Oceanography*, *178*(July 2018), 102,162, doi:10.1016/j.pocean.2019.102162.

Flemming, B. W., and K. Ziegler (1995), High-Resolution Grain Size Distribution Patterns and Textural Trends in the Backbarrier Environment of Spiekeroog Island (Southern North Sea), *Senckengbergiana Maritima*, *26*, 1–24.

Flores, R. P., S. Rijnsburger, A. R. Horner-Devine, A. J. Souza, and J. D. Pietrzak (2017), The impact of storms and stratification on sediment transport in the Rhine region of freshwater influence, *Journal of Geophysical Research: Oceans*, *122*(5), 4456–4477, doi:10.1002/2016JC012362.

Flores, R. P., S. Rijnsburger, S. Meirelles, A. R. Horner-Devine, A. J. Souza, J. D. Pietrzak, M. Henriquez, and A. J. Reniers (2018), Wave generation of gravity-driven sediment flows on a predominantly sandy seabed, *Geophysical Research Letters*, *45*(15), 7634–7645, doi:10.1029/2018GL077936.

Fugate, D. C., and C. T. Friedrichs (2002), Determining concentration and fall velocity of estuarine particle populations using adv, obs and lisst, *Continental Shelf Research*, *22*(11-13), 1867–1886, doi:10.1016/S0278-4343(02)00043-2.

Green, M. O., and J. D. Boon (1993), The measurement of constituent concentrations in nonhomogeneous sediment suspensions using optical backscatter sensors, *Marine Geology*, *110*(1-2), 73–81, doi:10.1016/0025-3227(93)90106-6.

Green, M. O., R. G. Bell, T. J. Dolphin, and A. Swales (2000), Silt and sand transport in a deep tidal channel of a large estuary (Manukau Harbour, New Zealand), *Marine Geology*, *163*(1-4), 217–240, doi:10.1016/S0025-3227(99)00102-4.

Ha, H. K., W. Y. Hsu, J. P. Maa, Y. Y. Shao, and C. W. Holland (2009), Using ADV backscatter strength for measuring suspended cohesive sediment concentration, *Continental Shelf Research*, *29*(10), 1310–1316, doi:10.1016/j.csr.2009.03.001.

Hawley, N. (2004), A comparison of suspended sediment concentrations measured by acoustic and optical sensors, *Journal of Great Lakes Research*, *30*(2), 301–309, doi:10.1016/S0380-1330(04)70348-2.

Hendriks, H. C., B. C. van Prooijen, S. G. Aarninkhof, and J. C. Winterwerp (2020), How human activities affect the fine sediment distribution in the Dutch Coastal Zone seabed, *Geomorphology*, *367*, 107,314, doi:10.1016/j.geomorph.2020.107314.

Hoitink, A. J., and P. Hoekstra (2005), Observations of suspended sediment from ADCP and OBS measurements in a mud-dominated environment, *Coastal Engineering*, *52*(2), 103–118, doi:10.1016/j.coastaleng.2004.09.005.

Lavelle, J. W., H. O. Mofjeld, and E. T. Baker (1984), An in situ erosion rate for a fine-grained marine sediment., doi:10.1029/JC089iC04p06543.

Lenstra, K. J., S. R. Pluis, W. Ridderinkhof, G. Ruessink, and M. van der Vegt (2019), Cyclic channel-shoal dynamics at the Ameland inlet: the impact on waves, tides, and sediment transport, *Ocean Dynamics*, *69*(4), 409–425, doi:10.1007/s10236-019-01249-3.

Lin, J., Q. He, L. Guo, B. C. van Prooijen, and Z. B. Wang (2020), An integrated optic and acoustic (IOA) approach for measuring suspended sediment concentration in highly turbid environments, *Marine Geology*, *421*(October 2019), 106,062, doi:10.1016/j.margeo.2019.106062.

Many, G., X. Durrieu de Madron, R. Verney, F. Bourrin, P. R. Renosh, F. Jourdin, and A. Gangloff (2019), Geometry, fractal dimension and settling velocity of flocs during flooding conditions in the Rhône ROFI, *Estuarine, Coastal and Shelf Science*, *219*(January), 1–13, doi:10.1016/j.ecss.2019.01.017.

Moura, M. G., V. S. Quaresma, A. C. Bastos, and P. Veronez (2011), Field observations of SPM using ADV, ADP, and OBS in a shallow estuarine system with low SPM concentration-Vitória Bay, SE Brazil, *Ocean Dynamics*, *61*(2-3), 273–283, doi:10.1007/s10236-010-0364-5.

Nortek AS (2005), Vector Current Meter - User Manual, *Tech. Rep. N 300-100 Rev. H*, Nortek Group, Vangkroken, Norway.

Nortek AS (2008), Aquadopp High Resolution - User Manual, *Tech. Rep. AHR00-0101-0508*, Nortek AS, Vangkroken, Norway.

Öztürk, M. (2017), Sediment size effects in acoustic doppler velocimeter-derived estimates of suspended sediment concentration, *Water (Switzerland)*, *9*(7), doi:10.3390/w9070529.

Pearson, S. G., B. van Prooijen, F. de Wit, H. Meijer-Holzhauer, A. de Looff, and Z. B. Wang (2019), Observations of Suspended Particle Size Distribution on an Energetic Ebb-Tidal Delta, *Coastal Sediments 2019*, pp. 1991–2003, doi:10.1142/9789811204487_0172.

Pomázi, F., and S. Baranya (2020), Comparative assessment of fluvial suspended sediment concentration analysis methods, *Water*, *12*(3), doi:10.3390/w12030873.

Pomeroy, A. W., C. D. Storlazzi, K. J. Rosenberger, R. J. Lowe, J. E. Hansen, and M. L. Buckley (2021), The contribution of currents, sea?swell waves, and infragravity waves to suspended?sediment transport across a coral reef?lagoon system., *Journal of Geo-*

physical Research: Oceans, pp. 1–26, doi:10.1029/2020jc017010.

Postma, H. (1961), Suspended Matter and Secchi Disc Visibility in Coastal Waters, *Netherlands Journal of Sea Research*, *1*(3), 359–390.

Reniers, A. J., F. P. de Wit, M. F. S. Tissier, S. G. Pearson, L. B. Brakenhoff, M. van der Vegt, J. Mol, and B. C. van Prooijen (2019), Wave-Skewness and Current-Related Ebb-Tidal Sediment Transport: Observations and Modeling, in *Coastal Sediments 2019*, pp. 2018–2028, St. Petersburg, Florida, doi:10.1142/9789811204487_0174.

Rijkswaterstaat (1999), *Sedimentatlas Waddenzee*, 36–38 pp., Rijkswaterstaat, Haren, Netherlands.

Salehi, M., and K. Strom (2011), Using velocimeter signal to noise ratio as a surrogate measure of suspended mud concentration, *Continental Shelf Research*, *31*(9), 1020–1032, doi:10.1016/j.csr.2011.03.008.

Seapoint Sensors Incorporated (2013), Seapoint turbidity meter user manual, *Tech. rep.*, Seapoint Sensors, Inc, Exeter, NH.

Son, C. S., B. W. Flemming, and A. Bartholomä (2011), Evidence for sediment recirculation on an ebb-tidal delta of the East Frisian barrier-island system, southern North Sea, *Geo-Marine Letters*, *31*(2), 87–100, doi:10.1007/s00367-010-0217-8.

Soulsby, R. L. (1997), *Dynamics of marine sands: a manual for practical applications*, Thomas Telford.

Su, M., P. Yao, Z. B. Wang, C. Zhang, Y. Chen, and M. J. Stive (2016), Conversion of electro-optical signals to sediment concentration in a siltâĂŞsand suspension environment, *Coastal Engineering*, *114*, 284–294, doi:10.1016/j.coastaleng.2016.04.014.

Sutherland, T. F., P. M. Lane, C. L. Amos, and J. Downing (2000), The calibration of optical backscatter sensors for suspended sediment of varying darkness levels, *Marine Geology*, *162*(2-4), 587–597, doi:10.1016/S0025-3227(99)00080-8.

Thorne, P. D., and D. M. Hanes (2002), A review of acoustic measurement of small-scale sediment processes, *Continental Shelf Research*, *22*(4), 603–632, doi:10.1016/S0278-4343(01)00101-7.

Thorne, P. D., and D. Hurther (2014), An overview on the use of backscattered sound for measuring suspended particle size and concentration profiles in non-cohesive inorganic sediment transport studies, *Continental Shelf Research*, *73*, 97–118, doi: 10.1016/j.csr.2013.10.017.

Thorne, P. D., and R. Meral (2008), Formulations for the scattering properties of suspended sandy sediments for use in the application of acoustics to sediment transport processes, *Continental Shelf Research*, *28*(2), 309–317, doi:10.1016/j.csr.2007.08.002.

Thorne, P. D., P. J. Hardcastle, and R. L. Soulsby (1993), Analysis of Acoustic Measurements of Suspended Sediments, *Journal of Geophysical Research*, *98*(92), 899–910.

Thorne, P. D., I. D. Lichtman, and D. Hurther (2021), Acoustic scattering characteristics and inversions for suspended concentration and particle size above mixed sand and mud beds, *Continental Shelf Research*, *214*(November 2020), 104,320, doi: 10.1016/j.csr.2020.104320.

van de Kreeke, J., and A. Hibma (2005), Observations on silt and sand transport in the throat section of the Frisian Inlet, *Coastal Engineering*, *52*(2), 159–175, doi: 10.1016/j.coastaleng.2004.10.002.

Van Der Hout, C. M., R. Witbaard, M. J. N. Bergman, G. C. A. Duineveld, M. J. C. Rozemeijer, and T. Gerkema (2017), The dynamics of suspended particulate matter (SPM) and chlorophyll- a from intratidal to annual time scales in a coastal turbidity maximum, *Journal of Sea Research*, *127*(March), 105–118, doi: 10.1016/j.seares.2017.04.011.

van der Werf, J., J. A. Á. Antolínez, L. Brakenhoff, M. Gawehn, K. den Heijer, H. de Looff, R. Wilmink, M. van Maarsseveen, H. Meijer-Holzhauer, J.-W. Mol, S. G. Pearson, B. van Prooijen, G. Santinelli, C. Schipper, M. Tissier, P. K. Tonnon, L. de Vet, T. Vermaas, R. J. Wilmink, and F. de Wit (2019), Datareport Kustgenese 2.0., *Tech. Rep. 1220339-015-ZKS-0004*, Rijkswaterstaat, Delft, The Netherlands.

Van Prooijen, B. C., M. F. Tissier, F. P. De Wit, S. G. Pearson, L. B. Brakenhoff, M. C. Van Maarseveen, M. Van Der Vegt, J. W. Mol, F. Kok, H. Holzhauer, J. J. Van Der Werf, T. Vermaas, M. Gawehn, B. Grasmeijer, E. P. Elias, P. K. Tonnon, G. Santinelli, J. A. Antolínez, P. L. M. De Vet, A. J. Reniers, Z. B. Wang, C. Den Heijer, C. Van Gelder-Maas, R. J. Wilmink, C. A. Schipper, and H. De Looff (2020), Measurements of hydrodynamics, sediment, morphology and benthos on Ameland ebb-tidal delta and lower shoreface, *Earth System Science Data*, *12*(4), 2775–2786, doi:10.5194/essd-12-2775-2020.

Voulgaris, G., and S. T. Meyers (2004), Temporal variability of hydrodynamics, sediment concentration and sediment settling velocity in a tidal creek, *Continental Shelf Research*, *24*(15), 1659–1683, doi:10.1016/j.csr.2004.05.006.

Weeks, A. R., J. H. Simpson, and D. Bowers (1993), The relationship between concentrations of suspended particulate material and tidal processes in the Irish Sea, *Continental Shelf Research*, *13*(12), 1325–1334, doi:10.1016/0278-4343(93)90086-D.

WET Labs Inc (2019), User manual: ECO Fluorometers and Scattering Sensors, *Tech. rep.*, Philomath, OR.

WETLabs (2010), ECO 3-Measurement Sensor User's Guide, *Tech. rep.*, WET Labs, Inc., Philomath, OR.

Winkelmolen, A. M., and H. J. Veenstra (1974), Size and shape sorting in a Dutch tidal inlet, *Sedimentology*, *21*(1), 107–126, doi:10.1111/j.1365-3091.1974.tb01784.x.

YSI Incorporated (2012), *6-Series Multiparameter Water Quality Sondes User Manual*, revision j ed., 374 pp., YSI Incorporated, Yellow Springs, Ohio.

Zhu, Q., B. C. van Prooijen, D. C. Maan, Z. B. Wang, P. Yao, T. Daggers, and S. L. Yang (2019), The heterogeneity of mudflat erodibility, *Geomorphology*, *345*, doi:10.1016/j.geomorph.2019.106834.